K. Sekiyama^{1,2*}, S. Yamada¹, T. Nakagawa¹, Y. Nakayama², T. Kajiwara²

Partially Filled Flow Simulation Using Meshfree Method for High Viscosity Fluid in Plastic Mixer

A novel simulation technique for the flow in plastic mixers based on Element-free Galerkin Method (EFGM) has been developed in this study. To improve the simulation accuracy, a "rearrangement" scheme has been employed which eliminates errors caused by the irregular distribution of data points. Through several numerical tests, the new simulation technique has been validated to be applicable to high viscosity fluid flow with enough accuracy. Furthermore, simulation examples for realistic mixers were carried out using the developed technique. From the results, it was found that the developed technique is capable to investigate the relationship between flow behavior inside realistic mixers and operating conditions.

1 Introduction

Twin screw extruders and mixers have been used in polymer processing and for producing chemicals, because they have good mixing performance and provide mass-production. There are many studies to evaluate the mixing performance of extruders and mixers. Especially, flow simulations to understand flows inside extruders and mixers are useful to get detailed information like velocity and stress distributions.

Yang et al. (1992), for example, conducted a three-dimensional non-Newtonian flow analysis of the kneading disk region in a co-rotating twin-screw extruder on the basis of finite element method (hereinafter "FEM"). Kajiwara et al. (1996), on the other hand, conducted a three-dimensional non-Newtonian flow analysis on a melt-conveying zone in an intermeshed counter-rotating twin-screw extruder by FEM using the flow passage shape created by full-flight screws with a spiral angle. There are many other reports; however, most of them assume that flow passages are filled with melt, and very few analyses have been made on the flow in a partially filled state occurring in actual mixing.

Applying a mesh method, such as FEM, to the simulation of partially filled state requires extremely complicated processing of free surfaces whose shapes change with time, making practical analysis difficult. Against this background, mesh-free method has attracted attention in recent years. As shown in

Fig. 1, mesh-free method has no "mesh" and calculation points (nodes) can move freely along the flow. Thus, mesh-free methods eliminate the issues associated with meshing and have an advantage that they can solve large deformation problems involving free surfaces more easily than mesh methods. Fukuzawa et al. (2015) developed a simulation technique for highly viscous non-Newtonian fluids on the basis of moving particle simulation (MPS) and analyzed the phenomena of molten resin flowing through a twin screw extruder in a partially filled state. Eitzlmayr et al. (2015a; 2015b) applied Smoothed Particle Hydrodynamics method (SPH) to study the flow and mixing in a conveying element of a co-rotating twin-screw extruder in partially filled states. However, the results of these flow predictions are still qualitative and have not yet led to quantitative evaluation. Against this background, this study has been conducted with the aim of improving the accuracy, so that the analyses based on a mesh-free method can be used for the designing of mixers in a sufficiently quantitative result.

When typical techniques of the mesh-free method including SPH (Monaghan, 1992) and MPS (Koshizuka and Oka, 1996) are applied to highly viscous fluid, a fatal error occurs in rigid body rotation. This problem, on the other hand, does not occur in the Element-free Galerkin method (EFGM) based on a weak form integral equation, because this method mainly handles the problems in structures with high stiffness and postulates high-order interpolation. In addition, velocity boundary conditions can be easily introduced without any complicated boundary treatment, such as the placement of special boundary particles as required by SPH and MPS.

Hence, in this study, EFGM is applied to partially filled flow of molten plastic with the aim of improving the accuracy. Furthermore, a new scheme keeping distances among data points is introduced to improve simulation accuracy. As validation, the simulation results are compared with the experimental results. Moreover, partially filled flow simulations in realistic plastic mixers are carried out using the developed simulation method.

2 Simulation Method

2.1 Governing Equation

This study has been conducted based on the following assumptions. The material is a viscous body that is almost incompres-

¹Mechanical Engineering Research Laboratory, Kobe Steel, Ltd., Hyogo, Japan

²Department of Chemical Engineering, Faculty of Engineering, Kyushu University, Fukuoka, Japan

^{*} Mail address: Kazuhide Sekiyama, Kobe Steel, Ltd., 1-5-5 Takatsukadai, Nishi-ku, Kobe, Hyogo, 651-2271, Japan E-mail: Sekiyama.kazuhide@kobelco.com

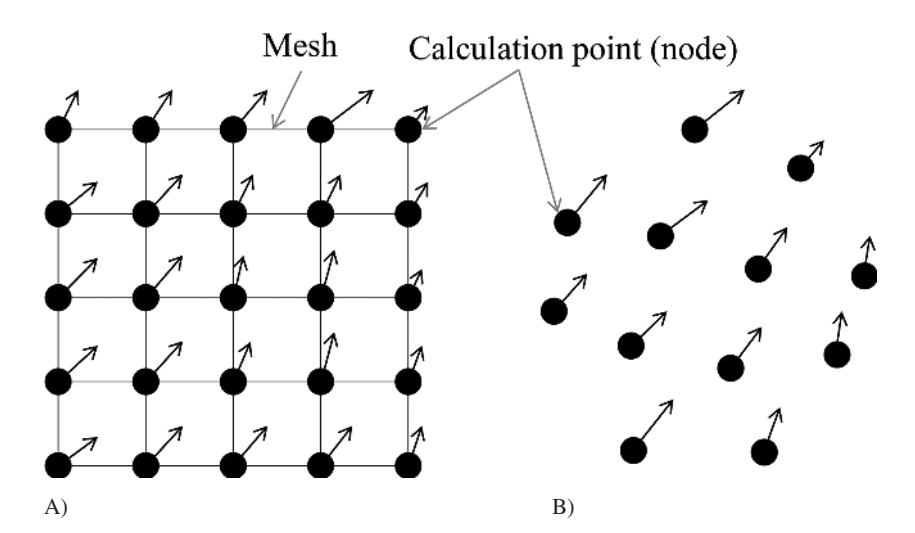


Fig. 1. Mesh method (A) and mesh-free meth-

sible in isothermal conditions, in which the viscosity is a function of only strain rate. The equation of motion is given as fol-

$$\rho \dot{\mathbf{u}} = \nabla \cdot \mathbf{\sigma} + \mathbf{b} \quad \text{in } \Omega, \tag{1}$$

$$\mathbf{n} \cdot \mathbf{\sigma} = \overline{\mathbf{t}} \quad \text{in } \Gamma_{\mathbf{t}},$$
 (2)

$$\mathbf{u} = \bar{\mathbf{u}} \quad \text{in } \Gamma_{\mathbf{u}}, \tag{3}$$

$$\sigma_{ij} = 2\mu \dot{\epsilon}'_{ij} + \lambda \dot{\epsilon}_{\nu} \delta_{ij}, \tag{4}$$

where: Ω , object domain; Γ_t , boundary prescribing surface force; Γ_{u} ; ρ , density of fluid; $\dot{\mathbf{u}}$, time differential velocity vector; boundary prescribing velocity; σ , stress tensor; **b**, body force vector; ∇ , vector differential operator; \mathbf{u} , velocity vector; \mathbf{n} , vector normal to boundary; $\bar{\mathbf{u}}$, boundary velocity vector; and $\bar{t},$ surface force vector. $\sigma_{ij}, \dot{\epsilon}'_{ij}, \dot{\epsilon}_v,$ stress, strain deviator, volumetric strain respectively; μ , viscosity of fluid; λ , a resistance coefficient to volume change and enough large against fluid viscosity. δ_{ii}; Kronecker delta. The velocity boundary condition is derived from the penalty method.

2.2 Approximation of Velocity Field Based on MLS Interpolation

In the EFGM, the velocity component at an arbitrary point of a continuum body is expressed by a moving least squares interpolation (hereinafter MLS interpolation) as follows. Firstly, the following polynomial equation is defined:

$$\varphi(\mathbf{x}) = \mathbf{p}^{\mathrm{T}}(\mathbf{x})\mathbf{a}(\mathbf{x}),\tag{5}$$

where suffix T indicates transposition, $\mathbf{p}(\mathbf{x})$ is the base vector of a polynomial of degree m and $\mathbf{a}(\mathbf{x})$ is a coefficient vector. In the case of two dimensions, the following holds:

$$m = 0$$
: $\mathbf{p}^{T}(\mathbf{x}) = [1], \quad \mathbf{a}(\mathbf{x}) = [a_1(\mathbf{x})],$ (6a)

$$m = 1: \quad \boldsymbol{p}^{T}(\boldsymbol{x}) = [1, x, y], \quad \boldsymbol{a}(\boldsymbol{x}) = [a_{1}(\boldsymbol{x}), \ a_{2}(\boldsymbol{x}), \ a_{3}(\boldsymbol{x})]^{T}. \qquad w_{I}(\boldsymbol{x}) = \begin{cases} \frac{e^{-\alpha(r/r_{0})^{2}} - e^{-\alpha}}{1 - e^{-\alpha}} \ , \ r \leq r_{0} \\ 0 \ , \ r > r_{0} \end{cases},$$

Next, in order to determine a, residual J(x) is defined as fol-

$$J(\mathbf{x}) = \sum_{I=1}^{n} w_{I}(\mathbf{x}) \left[\mathbf{P}^{T}(\mathbf{x}_{I}) \mathbf{a}(\mathbf{x}) - \phi_{I} \right]^{2}, \tag{7}$$

where $w_I(\mathbf{x})$ is a weight function, n is the number of nodes within the influence domain, and suffix I indicates the value for node I (a discretization point). J(x) represents weighted squared sum of the differences between $\varphi(\mathbf{x}_I)$ and φ_I . Minimizing this makes a to be expressed as follows:

$$\mathbf{a}(\mathbf{x}) = \mathbf{A}^{-1}(\mathbf{x})\mathbf{B}(\mathbf{x})\mathbf{\varphi},\tag{8}$$

where

$$\mathbf{\phi}^{\mathrm{T}} = [\mathbf{\phi}_{1}, \mathbf{\phi}_{2}, \cdots, \mathbf{\phi}_{N}], \tag{9}$$

$$\mathbf{A}(\mathbf{x}) = \sum_{I=1}^{n} \mathbf{w}_{I}(\mathbf{x}) \mathbf{p}(\mathbf{x}_{I}) \mathbf{p}^{T}(\mathbf{x}_{I}), \tag{10}$$

$$\mathbf{B}(\mathbf{x}) = [\mathbf{w}_1(\mathbf{x})\mathbf{p}(\mathbf{x}_1), \cdots, \mathbf{w}_n(\mathbf{x})\mathbf{p}(\mathbf{x}_n)]. \tag{11}$$

Further, Eq. 8 is incorporated into Eq. 5 to provide the following:

$$\varphi(\mathbf{x}) = \mathbf{N}(\mathbf{x})\varphi,\tag{12}$$

where

$$\mathbf{N}(\mathbf{x}) = \mathbf{p}^{\mathrm{T}}(\mathbf{x})\mathbf{A}^{-1}(\mathbf{x})\mathbf{B}(\mathbf{x}),\tag{13}$$

and N(x) corresponds to the shape function in FEM. Equation 13 is differentiated with respect to **X**, which provides the following equations:

$$\mathbf{\phi}_{i} = \mathbf{N}_{i}\mathbf{\phi},\tag{14}$$

$$\mathbf{N}_{.i} = \mathbf{p}_{.i}^{\mathrm{T}} \mathbf{A}^{-1} \mathbf{B} + \mathbf{p}^{\mathrm{T}} \mathbf{A}_{.i}^{-1} \mathbf{B} + \mathbf{p}^{\mathrm{T}} \mathbf{A}^{-1} \mathbf{B}_{.i}, \tag{15}$$

where suffix (i) indicates differentiation with respect to x, y or z. It should be noted that the following equation is used as a weight function:

$$w_{I}(\mathbf{x}) = \begin{cases} \frac{e^{-\alpha(r/r_{0})^{2}} - e^{-\alpha}}{1 - e^{-\alpha}}, & r \leq r_{0} \\ 0, & r > r_{0} \end{cases}$$
(16)

where $r = |\mathbf{X} - \mathbf{X}_I|$, α is a constant and r_0 is the radius of the domain of influence. The example calculation assumes $\alpha = 7$ and r_0 is a factor 2.6 larger than the initial inter-node distance.

2.3 Discretization

The velocity of an arbitrary point is expressed as follows based on Eq. 12:

$$u(\boldsymbol{x}) = \sum_{I=1}^{n} N_{I}(\boldsymbol{x}) \tilde{u}_{I}, \tag{17}$$

where N_I is the I^{th} component of N vector, u is the velocity inx direction and $\widetilde{u_I}$ is the velocity of node I in the same direction (the same applies to other directions). Using the above equations, the governing equations are discretized to the following equations:

$$\mathbf{K}\tilde{\mathbf{u}} = \mathbf{f},\tag{18}$$

$$\mathbf{K}_{IJ} = \int_{\Omega} \mathbf{B}_{I}^{T} \mathbf{D} \mathbf{B}_{J} d\Omega + k \int_{\Gamma_{IJ}} \mathbf{N}_{I}^{T} \mathbf{N}_{J} d\Gamma, \tag{19}$$

$$\mathbf{f}_{\mathrm{I}} = \int_{\Omega} N_{\mathrm{I}} \mathbf{b} d\Omega + \int_{\Gamma_{\mathrm{I}}} N_{\mathrm{I}} \overline{\mathbf{t}} d\Gamma + k \int_{\Gamma_{\mathrm{I}}} N_{\mathrm{I}} \overline{\mathbf{u}} d\Gamma, \tag{20}$$

where $\tilde{\mathbf{u}}$ represents the velocity vector, suffixes I and J indicate components for node I and J respectively. In the case of a two-dimensional problem, each matrix component is expressed as follows:

$$\mathbf{B}_{\rm I} = \begin{bmatrix} N_{\rm I,x} & 0\\ 0 & N_{\rm I,y}\\ N_{\rm I,y} & N_{\rm I,x} \end{bmatrix},\tag{21}$$

$$\mathbf{N}_{I} = \begin{bmatrix} N_{I} & 0\\ 0 & N_{I} \end{bmatrix}, \tag{22}$$

$$\mathbf{D} = \begin{bmatrix} 4\mu/3 + \lambda & -2\mu/3 + \lambda & 0\\ -2\mu/3 + \lambda & 4\mu/3 + \lambda & 0\\ 0 & 0 & \mu \end{bmatrix}, \tag{23}$$

where μ is the viscosity. These matrices correspond to the following relational expressions (stress and strain rate are expressed in vectors):

$$\mathbf{\sigma} = \left[\sigma_{\mathbf{x}}, \sigma_{\mathbf{y}}, \tau_{\mathbf{x}\mathbf{y}}\right]^{\mathrm{T}},\tag{24}$$

$$\dot{\boldsymbol{\epsilon}} = \left[\dot{\epsilon}_x, \dot{\epsilon}_y, \dot{\gamma}_{xy}\right]^T = \left[\partial u/\partial x, \partial v/\partial y, \partial u/\partial y + \partial v/\partial x\right]^T, \quad (25)$$

$$\mathbf{\sigma} = \mathbf{D}\dot{\mathbf{\varepsilon}},\tag{26}$$

$$\dot{\mathbf{\epsilon}} = \mathbf{B}\tilde{\mathbf{u}} = \sum_{I}^{\Omega} \mathbf{B}_{I}\tilde{\mathbf{u}}_{I},\tag{27}$$

$$\tilde{\mathbf{u}}_{I} = \begin{bmatrix} \tilde{\mathbf{u}}_{I} & \tilde{\mathbf{v}}_{I} \end{bmatrix}^{T}, \tag{28}$$

As a result of this processing, the equation of continuity is almost fully satisfied.

2.4 Integration Method

In general, the EFGM requires cells for numerical integration (Belytschko et al., 1994), a factor that increases the calculation load. Hence, integration points are made to conform to node points (Beissel and Belytschko, 1996; Chen et al., 2001) to eliminate the need for integration cells. In this case, Eqs. 19 and 20 respectively become as follows:

$$\begin{aligned} \boldsymbol{K}_{IJ} &\cong \sum_{a}^{\Omega} \boldsymbol{B}_{I}(\boldsymbol{x}_{a})^{T} \boldsymbol{D}(\boldsymbol{x}_{a}) \boldsymbol{B}_{J}(\boldsymbol{x}_{a}) \boldsymbol{V}_{a} + \kappa \sum_{a}^{\Gamma_{u}} \boldsymbol{N}_{I}(\boldsymbol{x}_{a})^{T} \boldsymbol{N}_{J}(\boldsymbol{x}_{a}) \boldsymbol{S}_{a}^{u}, \end{aligned} \tag{29}$$

$$\begin{split} \mathbf{f}_{\mathrm{I}} &\cong \sum_{a}^{\Omega} N_{\mathrm{I}}(\mathbf{x}_{a}) \mathbf{b}(\mathbf{x}_{a}) V_{a} + \sum_{a}^{\Gamma_{\mathrm{t}}} N_{\mathrm{I}}(\mathbf{x}_{a}) \bar{\mathbf{t}}(\mathbf{x}_{a}) S_{a}^{\mathrm{t}} \\ &+ \kappa \sum_{a}^{\Gamma_{\mathrm{u}}} N_{\mathrm{I}}(\mathbf{x}_{a}) \bar{\mathbf{u}}(\mathbf{x}_{a}) S_{a}^{\mathrm{u}}, \end{split} \tag{30}$$

where V_a is the volume occupied by node a, and S_a^u and S_a^t respectively represent the areas on Γ_u and Γ_t occupied by node a. Although the \sum_a^Ω in the above equation formally applies to all the nodes, $\mathbf{B}_I(\mathbf{x}_a) = 0$ and $\mathbf{N}_I(\mathbf{x}_a) = 0$ hold at points I outside the domain of influence of node a. Therefore, only the sum inside the domain of influence must be calculated. Further, κ is a penalty number, which allows making $S_a^u = 1$.

Now, for convenience, V_a is calculated by the following equation under an assumption that the initial nodes are arranged equally spaced:

$$V_a = \begin{cases} \frac{V_t}{n_f + n_b/2} & \text{fluid} \\ \frac{1}{2} \frac{V_t}{n_f + n_b/2} & \text{boundary} \end{cases}, \tag{31}$$

where V_t is the total volume of the fluid, n_f is the number of fluid nodes and n_b is the number of boundary nodes. In the equation, the volume of the boundary nodes is regarded as half that of fluid nodes.

It should be noted that no processing was performed to suppress the pressure oscillation associated with the nodal integration.

2.5 Time Marching Method

A fully implicit method is used for determining node velocity, while the coordinates are updated by a secondary Runge-Kutta method. The following describes the procedure:

Step 1:
$$\mathbf{p}^{T}(\mathbf{x}) = [1], \ \tilde{\mathbf{u}}_{t} = \mathbf{K}(\mathbf{X}_{t}, t)^{-1} \mathbf{f}(\mathbf{X}_{t}, t),$$

$$\mathbf{a}(\mathbf{x}) = [\mathbf{a}_1(\mathbf{x})],\tag{32}$$

Step 2: Determining the interpolation speed U_t of nodes by Eq. 17,

Step 3:
$$\mathbf{X}_{t+\Delta t/2} = \mathbf{X}_t + \frac{1}{2}\Delta t \mathbf{U}_t$$
, (33)

Step 4:
$$\tilde{\mathbf{u}}_{t+\Delta t/2} = \mathbf{K} \left(\mathbf{X}_{t+\Delta t/2}, t + \frac{1}{2} \Delta t \right)^{-1} \mathbf{f} \left(\mathbf{X}_{t+\Delta t/2}, t + \frac{1}{2} \Delta t \right),$$
(34)

Step 5: Determining the interpolation speed $U_{t+\Delta t/2}$ of nodes by Eq. 17,

Step 6:
$$\mathbf{X}_{t+\Delta t} = \mathbf{X}_t + \Delta t \mathbf{U}_{t+\Delta t/2},$$
 (35)

where suffix t indicates values at time t, while Δt is the time step size.

In the case where μ depends on strain rate, it would be most accurate if the strain rate was calculated after Step 6 to make a correction to μ and if the calculations were repeated from Step 1 without progression of time until the variation of μ becomes equal to or smaller than an allowable value. Here, however, for the purpose of simplifying the algorithm, μ for the strain rate at the previous time step is used as an approximate value, and the calculations are not repeated.

The viscosity of plastic that becomes the main application target of this study can be very high, in the order of $10^4 \, \text{Pa} \cdot \text{s}$ at maximum. Therefore, if an explicit method or a semi-implicit method was to be used for the time integration, the time step size satisfying the stability condition for diffusion number would become extremely small, resulting in an enormous amount of calculation time. Because of this, a fully implicit method, which is unconditionally stable, is used here.

2.6 New "Rearrangement" Scheme for Improving Calculation Accuracy

A common problem with the above mesh-free methods is the deterioration of accuracy caused by uneven inter-node distance (Belytschko et al., 1994). That is, in the case of mixing simulation, the fluid node arrangement is disturbed as the rotation proceeds, causing significant accuracy deterioration. In order to solve this problem, a new technique, called "rearrangement", has been devised. The following describes the procedures for discretization and calculation.

Step 0:
$$\hat{\mathbf{u}} = \mathbf{0}, \ \mathbf{X}_{\bar{t}=0} = \mathbf{X}_{t},$$
 (36)

Step 1: Calculating the force **Q** acting on the nodes by the following equations:

$$\mathbf{Q}_{\rm I} = \sum_{\rm J=1}^{\rm n} q_{\rm IJ} \frac{\mathbf{X}_{\rm J} - \mathbf{X}_{\rm I}}{|\mathbf{X}_{\rm J} - \mathbf{X}_{\rm I}|},\tag{37}$$

$$q_{IJ} = \begin{cases} k\delta_{IJ}, \, \delta_{IJ} < 0 \\ 0, \quad \delta_{IJ} \ge 0 \end{cases} \tag{38}$$

$$\delta_{IJ} = |\mathbf{X}_{J} - \mathbf{X}_{I}| - s_0, \tag{39}$$

Step 2: Updating the velocity and coordinates by the following equations (note: the coordinates of boundary nodes are determined by Eqs. 32 to 35):

$$\hat{\mathbf{u}}_{\bar{\mathbf{t}}+\Delta\bar{\mathbf{t}}} = \hat{\mathbf{u}}_{\bar{\mathbf{t}}} + \Delta\bar{\mathbf{t}}(\mathbf{Q} - c\hat{\mathbf{u}}_{\bar{\mathbf{t}}}),\tag{40}$$

$$\mathbf{X}_{\bar{\mathbf{t}} + \Lambda \bar{\mathbf{t}}} = \mathbf{X}_{\bar{\mathbf{t}}} + \Delta \bar{\mathbf{t}} \mathbf{u}_{\bar{\mathbf{t}} + \Lambda \bar{\mathbf{t}}},\tag{41}$$

where k is spring stiffness, c is damping factor, $\Delta \bar{t}$ is time step size and s_0 is collision detection distance. Steps 1 and 2 are repeated the number of times specified by the user or until the variation of δ_{IJ} becomes an allowable value, e.g. when all δ_{IJ} are larger than 0. In the following examples, we repeated the steps 32 times.

According to the above algorithm, a repulsive force works on the nodes when the inter-node distance becomes s_0 or smaller, making the nodes unlikely to cluster and to be arranged homogeneously as shown in Fig. 2. For two-dimensional cases, s_0 is given by the following:

$$s_0 = \sqrt{\frac{2}{\sqrt{3}} \frac{V_t}{n_f + n_b/2}},\tag{42}$$

That is, in a perfectly homogeneous arrangement, three neighboring nodes form an equilateral triangle, and s_0 represents the side length of a fluid volume equaling the summation of the triangular areas.

Further, k, c and $\Delta \bar{t}$ do not have any physical implications and can be determined arbitrarily. This study uses the following equation which is independent of unit system:

$$k = 0.25/(1 - \eta^2), \tag{43}$$

$$c = 2\eta\sqrt{k}, (0 < \eta < 1),$$
 (44)

where η is a viscosity constant. The above equation gives a natural period of 2π . Therefore, $\Delta \bar{t}$ can be set to an appropriate value of 2π or smaller. The following calculation example uses $\eta = 0.1$, $\Delta \bar{t} = \pi/8$.

The above processing alters the coordinates of nodes. Thus, unless the values of strain rates are updated, an error occurs

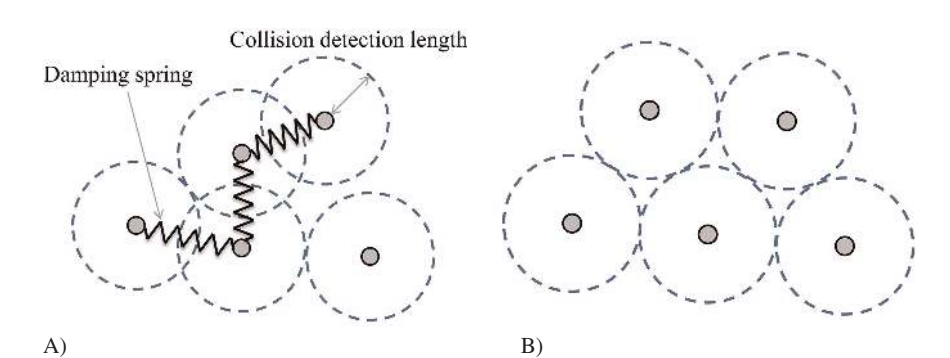


Fig. 2. Schematic views of the "rearrangement". Calculation points position before application (A), and after application (B)

for materials having dependence on strain rate. In addition, an error occurs which is caused by the free-surface shape being distorted by the non-physical rearrangement processing. In order to minimize these errors, and as the most convenient means, a small Δt is taken and a rearrangement is made for each step to minimize the coordinate variation per step.

3 Validation of Developed Method

In order to validate the accuracy and efficiency of this developed method, the simulation results are compared with experimental results on for a highly viscous fluid.

3.1 Comparison with Experiment on Rotating Cylinder

An experiment as shown in Fig. 3 was conducted using a rotation apparatus consisting of a cylindrical barrel and a cylindrical rotor. The apparatus was filled in half with silicon oil (KF-96H-100 Kcs, Shin-Etsu Chemical Co., Ltd., Tokyo, Japan). Then, the cylindrical rotor was rotated, and the behavior of the oil was observed in video. The results were compared with the analysis results. The experimental apparatus had dimensions of: barrel inner diameter, 50 mm; rotor diameter, 20 mm; rotor rotation velocity, 3 min⁻¹; and apparatus length, 90 mm. Since the cross-sectional shape is constant along the

longitudinal direction, a two-dimensional simulation was conducted. The conditions of the simulation were: with rearrangement; the number of fluid nodes, 3639; the number of boundary nodes, 442; the initial inter-node distance, 0.5 mm; Δt , 0.0556 s; density, 1000 kg/m³; the acceleration of gravity, 9.8 m/s; and viscosity, 100 Pa s.

Figure 4 shows the experimental results. Many bubbles were observed during the experiment (see Fig. 4A, C). Figure 4A is

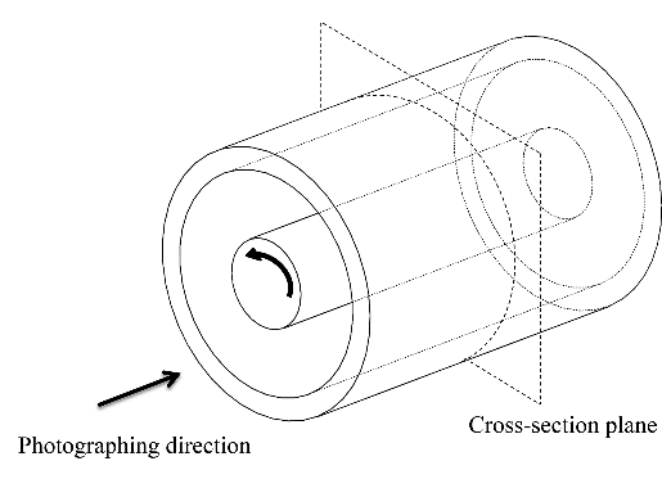


Fig. 3. The model of experiment on rotating cylinder

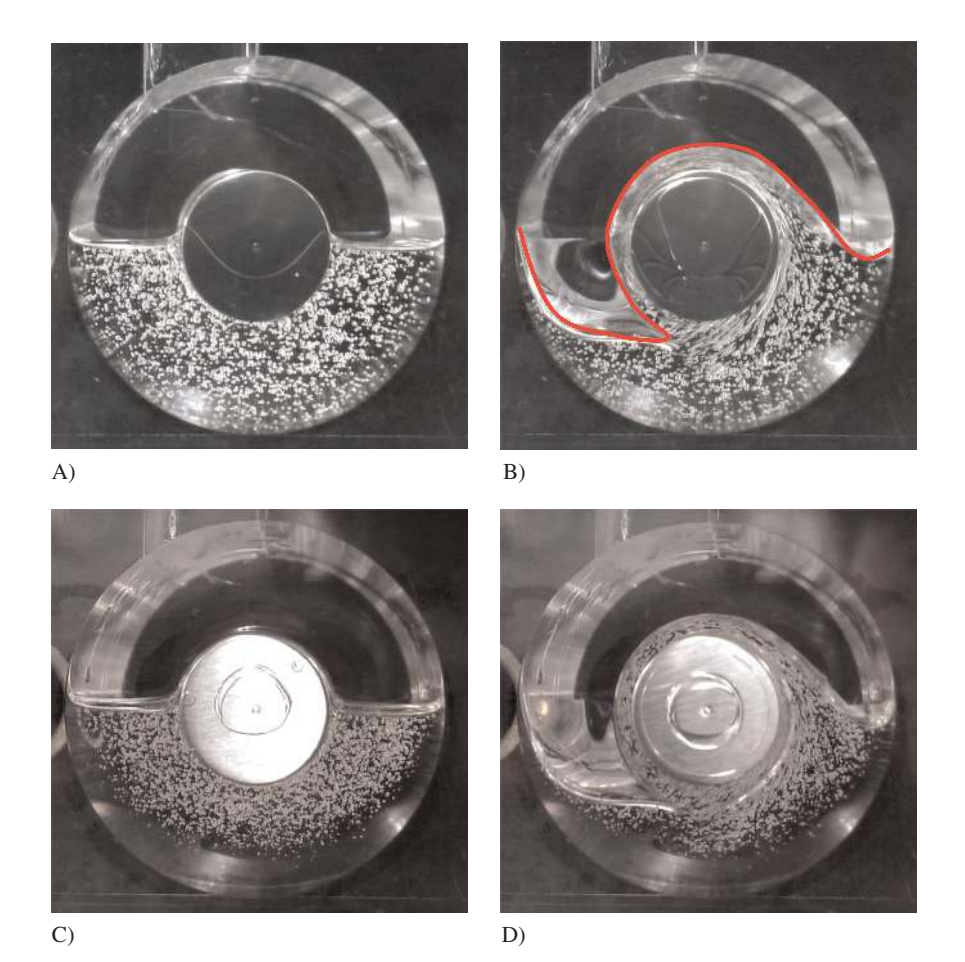


Fig. 4. Experimental results of rotating cylinder with bubbles (A, B), less bubbles (C, D), (A, C) initial state, (B, D) after 3 rotations. The red line in Fig. 4B shows the outline of free surface

a snapshot just after feeding the silicon oil into the barrel, Fig. 4C is a snapshot after leaving 15 h. However, as shown in Fig. 4C, an experiment conducted with less bubbles condition confirmed that these bubbles have little effect on the free surface shape of the fluid. Therefore, the free surface shape of experiment with bubbles is comparable with that of simulation. It is also to be noted that the viscosity represents the value measured for $\dot{\gamma} < 50~\text{s}^{-1}$ at the ambient temperature and can be regarded to be constant within the scope of this experiment.

Figure 5A shows the chronological change of node positions obtained by the simulation along with the experimental results. The red solid line in each diagram represents the contour, obtained from the corresponding photo, of the free surface. As shown by this figure, there is a good agreement in the shapes of the free surface. In the experiment, a steady state where the free-surface shape remains almost unchanged was achieved at one rotation. The simulation also shows a good agreement in the free-surface shapes after one rotation and three rotations, reproducing the steady state.

Figure 5 compares the results with and without rearrangement. In the case without rearrangement, the nodes are separated with the accuracy significantly deteriorating after one rotation, showing that the rearrangement processing is indispensable in this case. The CPU time required for this simulation was 528 s per rotation (i5-3210 M, 2.5 GHz, 1 core). The same calculation performed by an explicit method took a

factor of approximately 200 more CPU time than this solving method (fully implicit method). Actual resin mixing involves much higher viscosity, implying that the use of an implicit method is also indispensable.

3.2 Comparison with Experiment on Triangular-Shaped Rotor

A model mixer including a rotor with three tips (Hotani and Kuroda, 2009) was simulated and the simulation results were compared with experimental ones. Figure 6 shows the isometric view of the experimental model and the two-dimensional shape analyzed. Experiments were conducted using a rotor with a same cross-sectional shape as Fig. 6A. Initial fluid position of simulation is divided into three parts to obtain steady state quickly as shown in Fig. 6B. The rotor has no torsion in the axial direction to avoid the flow in the axial direction as much as possible. The rotor has an axial length of 89 mm, and the barrel has an axial length of 90 mm, leaving gaps of 1 mm in total at the axial ends.

The cylindrical barrel was partially (80%) filled with silicon oil (KF-96H-1 Mcs by Shin-Etsu Chemical Co., Ltd., Tokyo, Japan) and the triangular-shaped rotor was rotated. During the experiment, the torque acting on the rotor was measured, and the free-surface shape of the fluid was observed in video. The

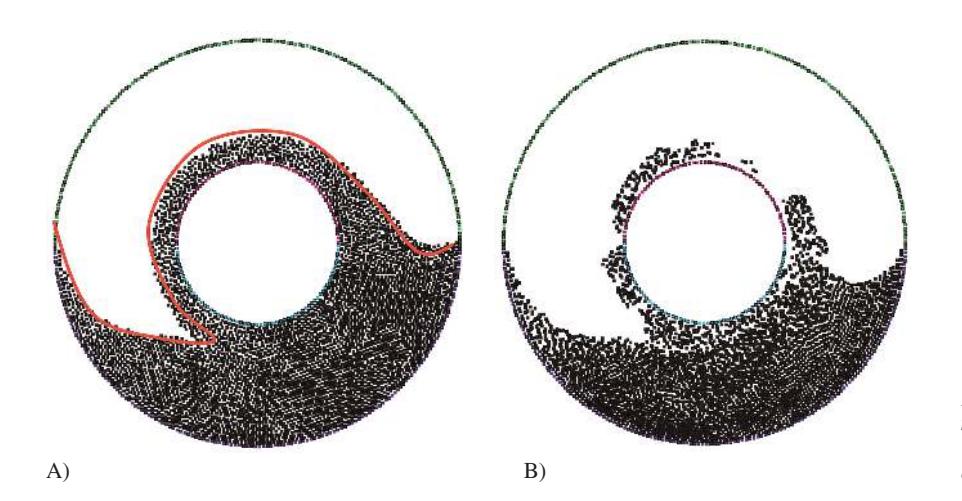


Fig. 5. Simulation results with "rearrangement" (A), and without "rearragement" (B). The red line shows the outline obtained from experimental result

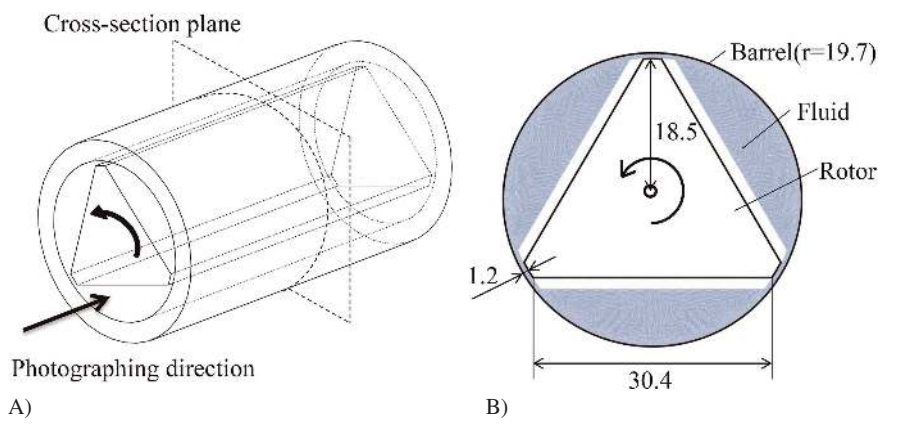


Fig. 6. The calculation and experimental model of triangular-shaped rotor. Isometric view of simple mixer (A), and cross-section model of initial state of simulation (B)

conditions of the simulation were: with node rearrangement; the number of fluid nodes, 23400; the number of boundary nodes, 2898; the initial inter-node distance, 0.2 mm; density, 1000 kg/m³. The smallest rotation speed is 3 min⁻¹ in these experiments. The interval time of each tips passage is 6.7 s. The fluid didn't deform by gravity while in the interval. The gravity was ignored in this simulation.

The highly viscous silicon oil used in this experiment is shown to exhibit shear thinning at high strain rates. In the simulation, the viscosity which is measured by a frequency viscometer was calculated by the following equation:

$$\mu = \left\{ \begin{array}{ll} 2491.72 \; \dot{\gamma}^{-0.4186} & , \; \mu > 1000 \\ 1000 & , \; \mu \leq 1000 \end{array} \right. \eqno(45)$$

Figure 7 compares the steady-state flow behaviors of the simulation and experiment (rotation velocity: 6 min⁻¹). The red solid lines in Fig. 7B are the contours, retrieved from the experimental results, of the free surface and represent the free surface shape at the center in the axial direction. As shown in this figure, the 3 separate fluid portions have roughly the same free-surface shape.

Figure 8 shows the torque measured for each number of revolutions in the simulation and experiment. This figure indicates that the analytical results ($T_{cal.}$) yield smaller torque than the experimental results ($T_{exp.}$).

A possible cause of this difference is as follows: The simulation was conducted on a two-dimensional model, while the experiment was performed on an apparatus having gaps between the axial end faces and the ends of rotor, as described above. Torque is also generated in these gaps. In addition, in the experiment, an axial flow occurs although slightly, which may cause the torque to be changed. Among these factors, the torque generated in the gaps between the axial ends and rotor ends can be calculated. The result reflecting this torque (Ttotal) is also shown in Fig. 8. It should be noted that, for simplifying the calculation, the triangular shape is converted to a circle having the same area, and the fluid is assumed to fill the entire gaps.

As demonstrated in Fig. 8, T_{total} agrees well with $T_{exp.}$, verifying the validity of this simulation.

4 Results and Discussion of Flow Simulation Inside Realistic Mixers

The partially filled simulation of the plastic mixer becomes possible using the developed method, so that it is possible to know the internal filling state which could not be achieved by the conventional fully filled simulation. Therefore, in this section, we investigate the change of the internal filling state with respect to the change of operating condition for continuous mixer with different rotor shapes.

4.1 Numerical Simulation Condition

We carried out partially filled simulations for melt mixing zones of counter-rotating continuous mixers shown in Fig. 9. The following describes the calculation models and conditions of the simulations. There are both screw zone and mixing zone in each calculation model. Regarding screw zones, both mod-

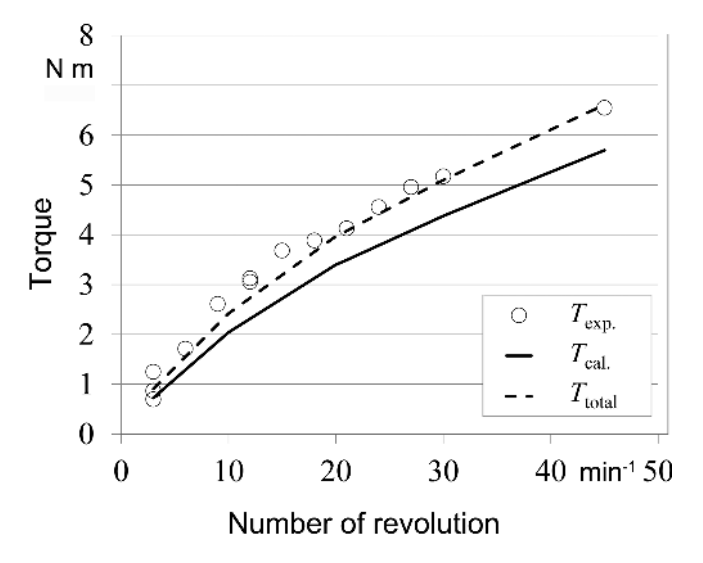
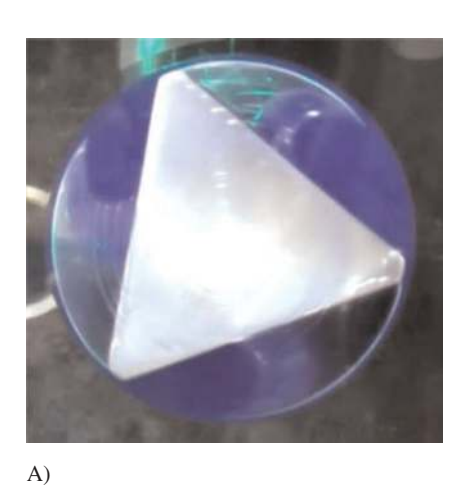


Fig. 8. Simulated torque acting on rotor vs. speed of revolution



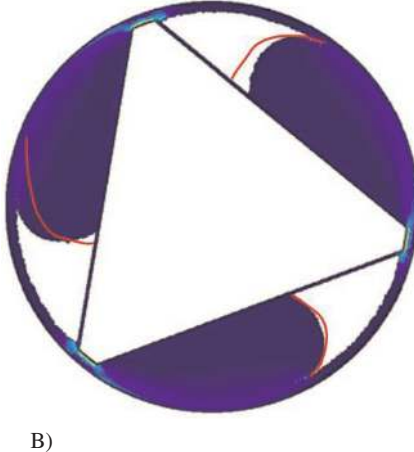


Fig. 7. Steady state flow condition at 6 min⁻¹ of experimental result (A), and simulation result (B). The red line shows the outline of free surface of experimental result

els have same screw shapes. Regarding the mixing zone, they have the same cross-sectional shape. The configurations are Model-FF (only forward rotor; Model-FB) forward and backward rotor. Nominal barrel diameter is 100 mm, mixing zone length is 144 mm, and barrel length is 254 mm. In this simulation, we use Newtonian viscosity. The viscosity is 1000 Pa s.

The density is 900 kg/m³. The rotation speeds were 200, 400, 600 min⁻¹. The feed rates were 185, 544, 907 kg/h. We investigated all combinations of two rotor shapes, three rotation speeds and three feed rates. The surface boundary condition is no slip. The outlet cross-sectional boundary condition is free outflow. The inlet cross-sectional boundary condition is con-

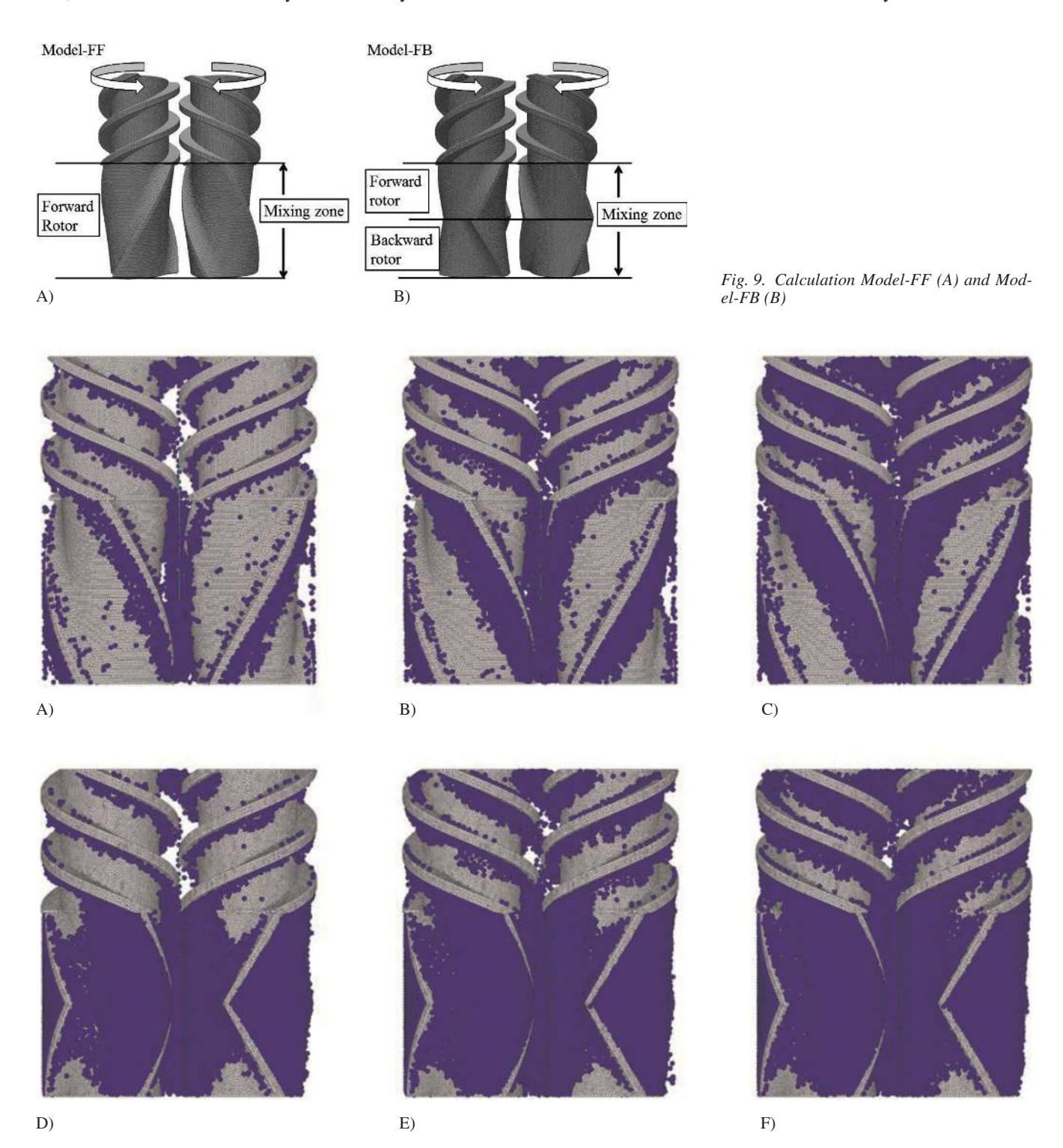


Fig. 10. Filling states of Model-FFs (upper) and Model-FBs (bottom) at 200 min⁻¹, A) Modell-FF 181 kg/h, B) Modell-FF 544 kg/h, C) Modell-FF 907 kg/h, D) Modell-FFs 181 kg/h, E) Modell-FFs 544 kg/h, F) Modell-FFs 907 kg/h

stant velocity. In the initial states of the simulations, mixers are empty. Fluid is fed from the upstream ends of the screw zones. The simulations are finished when the flow behaviors were constant.

4.2 Results and Discussion

4.2.1 Filling State and Filling Ratio Inside Mixer

We observed the filling state inside the mixers. The filling states at the rotation speed of 200 min⁻¹ obtained by the simulations are shown in Fig. 10 (the results of Model-FFs are shown at the top; those of Model-FBs are shown at the bottom).

In the cases of Model-FFs, polymer exists just only around the tips of the rotors. On the other hand, the mixing zones in Model-FBs are almost fully filled with the polymer. This feature of filling state appeared at other rotation speeds.

The relationship between the filling ratios against rotation speed and feed rates are summarized in Fig. 11 and 12. Filling ratios at feed rates of 185, 544, 907 kg/h are shown in Fig. 11. The filling ratios at rotation speeds of 200, 400, 600 min⁻¹ are

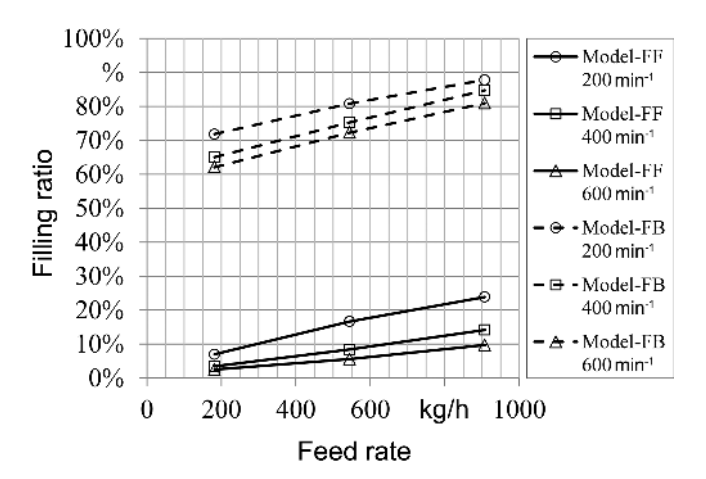


Fig. 11. Relationship between filling ratio and feed rate

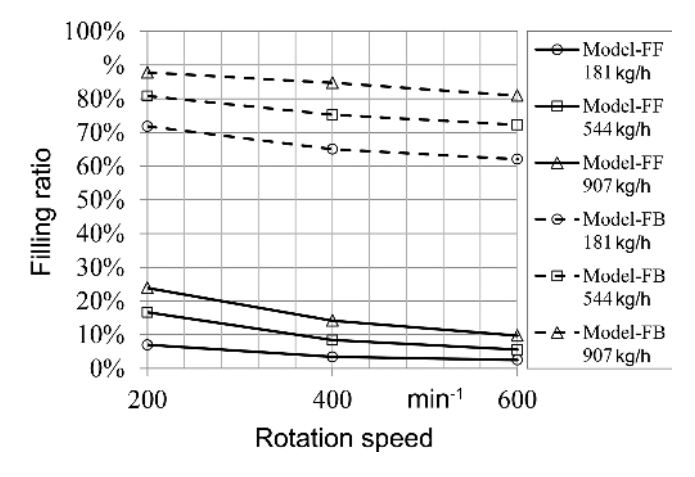


Fig. 12. Relationship between filling ratio and rotation speed

shown in Fig. 12. These results show that the filling ratios of Model-FBs are larger than those of Model-FFs in all cases. From this trend, it is mentioned that the backward rotor which generates flow resistance increases the filling ratio of the mixing zone.

Kim and White (1994), White and Chen (1994) and White et al. (2006) carried out experiments and simulations and mentioned that the screw is filled in the backward screw and the forward screw before them. On the other hand, in this simulation, Model-FBs are not fully filled even though they have backward rotors. The reason for this difference is the condition difference downstream of the backward rotor. Free outflow boundary condition is applied for outlet boundary in this simulation. Fluid near the outlet is easy to be out under this condition and filling ratios of Model-FBs are getting down to 65 to 85%. In the future, various outlet boundary conditions must be considered and discussed in detail.

As shown in Fig. 11, the larger the feed rate is, the higher the filling ratio is for all rotation speed cases. These results occur because pressure drops increased along with increasing feed rates. As shown in Fig. 12, the higher the rotation speed is, the lower the filling ratio is for all feed rate cases. These results occur because pumping capabilities are increased along with increasing of rotation speeds. Regarding Model-FFs, the pumping capabilities of both screw and mixing zones are increased because they have only forward torsion. Regarding Model-FBs, the pumping capabilities of mixing zone are not increased because the length of forward rotor and that of backward rotor is the same. In other words, only the screw zones have pumping capability for Model-FBs. From these results, it is found that the pumping capability of the screw zones affects the filling ratio of the mixing zone in the partially filled condition.

Lertwimolnun and Vergnes (2006) noted that the effects of feed rate Q and screw speed n are usually expressed through the ratio Q/n, which is proportional to the filling ratio of the screws. Figure 13 shows the relationship between the filling ratios and the ratio of feed rate and rotation speed Q/n. Regarding Model-FFs, there is a strong correlation between the filling ratio and Q/n. The larger the Q/n is, the higher the filling ratio is. In other words, the filling ratios of Model-FFs can be controlled by Q/n. Model-FFs are regarded as only forward screw because they have only forward torsion. Therefore, screw theo-

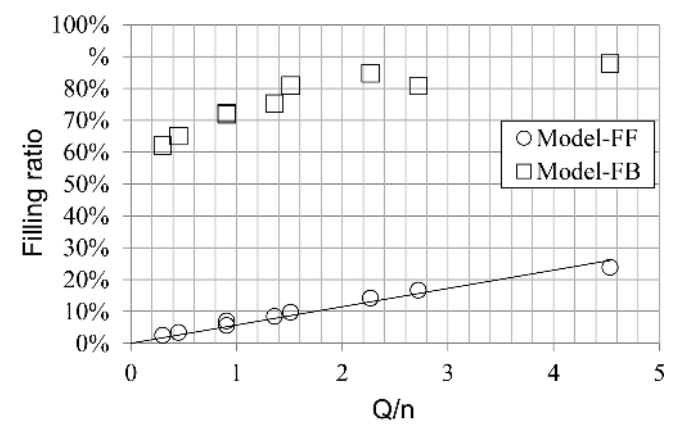


Fig. 13. Relationship between filling ratio and Q/n

ry can be applied, and the results are like screw results. On the other hand, regarding Model-FBs, it can be mentioned that there is a weaker correlation between the filling ratio and the Q/n than for Model-FFs. The effect of forward torsion is limited in Model-FBs as mentioned above. Therefore, it can be considered that the screw theory is not completely applied, and the correlation is weaker than for Model-FFs.

4.2.2 Average Residence Time

Average residence time (t_{ave}) is calculated by the equation shown below:

$$t_{ave} = 3600 \ \frac{\rho V_{mix}}{Q_{feed}}, \tag{46} \label{eq:46}$$

where ρ is density of fluid, V_{mix} is fluid volume inside mixing zone, Q_{feed} is feed rate in kg/h.

The average residence times at feed rates 185, 544, 907 kg/h are shown in Fig. 14. In both configurations, the larger the feed

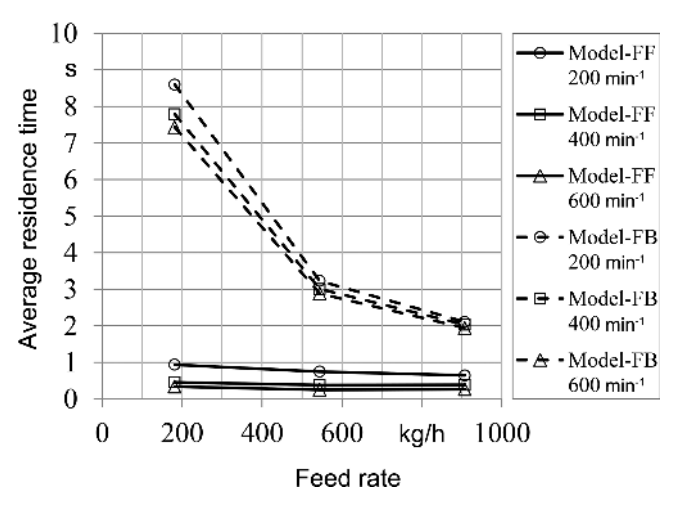


Fig. 14. Relationship between average residence time and feed rate

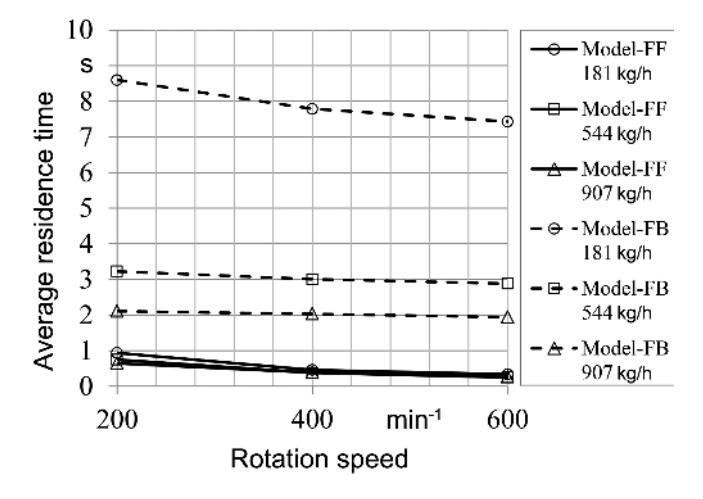


Fig. 15. Relationship between average residence time and rotation speed

rate is, the shorter the average residence time is. The average residence times of Model-FBs are longer than those of Model-FFs for all feed rates. From these results, it can be mentioned that the reduction of feed rate or the configuration which has backward rotor is one of the ways to obtain good mixing performance.

Average residence times at rotation speeds of 200, 400, 600 min⁻¹ are shown in Fig. 15. Regarding Model-FBs, the average residence time is almost constant in each feed rate. From the results shown in Fig. 14 and 15, the average residence times of Model-FB that have backward rotor are controllable by almost only feed rate.

From these results, we can say that the rotors with backward rotor can be appropriate for a mixing that needs longer residence time. It would lead to strong mixing. On the other hand, we can say the a rotors with only forward rotor can be appropriate for a mixing that needs shorter residence time. We can say that the configuration with only forward rotors strongly is related with feed rate and rotation speed. We conclude that the mixer shape and operating conditions are strongly related with the degree of mixing and we can predict the degree of mixing by using our simulation technique.

5 Conclusion

In the present work, a new simulation technique for partially filled flow has been developed. The mesh-free method has been employed and a new scheme called "rearrangement" has been proposed for partially filled simulations of plastic mixers. It is found that the scheme is effective to improve simulation accuracy and the developed simulation technique can predict partially filled flow phenomena with high accuracy.

Furthermore, the developed simulation technique has been used for realistic mixers to investigate the effects of rotation speed and feed rate on the filling state and average residence time. The investigation was carried out for two different mixing rotor shapes. From the results, it is found that our developed simulation technique is capable to reveal flow behaviors inside counter-rotating continuous mixers and the operating conditions that have strong correlation with the average residence time for each configuration. As a conclusion, it is found that our technique is useful to know flow phenomena inside mixer that is difficult to obtain by conventional simulation techniques.

In the future, we will clarify the stress distribution or the residence time distribution of partially filled state to investigate more detailed mixing conditions.

References

Beissel, S., Belytschko, T., "Nodal Integration of the Element-Free Galerkin Method", Comput. Methods Appl. Mech. Eng., **139**, 49–74 (1996), DOI:10.1016/S0045-7825(96)01079-1

Belytschko, T., Lu, Y. Y. and Gu, L., "Element-Free Galerkin Methods", Int. J. Numer. Methods Eng., **37**, 229–256 (1994), DOI:0029-5981/94/020229-28

Chen, J. S., Wu, C. T., Yoon, S. and You, Y., "A Stabilized Conforming Nodal Integration for Galerkin Mesh-Free Methods", Int. J. Numer. Methods Eng., 50, 435–466 (2001), DOI:10.1002/1097-0207(20010120)

- Eitzlmayr, A., Khinast, J., "Co-Rotating Twin-Screw Extruders: Detailed Analysis of Conveying Elements Based on Smoothed Particle Hydrodynamics. Part 1: Hydrodynamics", Chem. Eng. Sci., 134, 861–879 (2015a), DOI:10.1016/j.ces.2015.04.055
- Eitzlmayr, A., Khinast, J., "Co-Rotating Twin-Screw Extruders: Detailed Analysis of Conveying Elements Based on Smoothed Particle Hydrodynamics. Part 2: Mixing", Chem. Eng. Sci., 134, 880–886 (2015b), DOI:10.1016/j.ces.2015.05.035
- Fukuzawa, Y., Tomiyama, H. and Shibata, K., "Numerical Analysis of Polymer Fluid Flow Using the MPS Method", JSW Technical Review (in Japanese), 57–62 (2015)
- Hotani, S., Kuroda, Y., "Continuous Mixers for Resin", Kobe Steel Engineering Reports, 59, (2009)
- Kajiwara, T., Nagashima, Y., Nakano, Y. and Funatsu, K., "Numerical Study of Twin-Screw Extruders by Three-Dimensional Flow Analysis-Development of Analysis Technique and Evaluation of Mixing Performance for Full Flight Screws", Polym. Eng. Sci., 36, 2142–2152 (1996), DOI:10.1002/pen.10611
- Kim, P. J., White, J. L., "Flow Visualization and Residence Time Distributions in a Modular Co-rotating Twin Screw Extruder", Int. Polym. Proc., 9, 108–118 (1994), DOI:10.3139/217.940108
- Koshizuka, S., Oka, Y., "Moving-Particle Semi-Implicit Method for Fragmentation of Incompressible Fluid", Nucl. Sci. Eng., 123, 421–434 (1996), DOI:10.13182/NSE96-A24205
- Lertwimolnun, W., Vergnes, B., "Effect of Processing Conditions on the Formation of Polypropylene/Organoclay Nanocomposites in a Twin Screw Extruder", Polym. Eng. Sci., 46, 314–323 (2006), DOI:10.1002/pen.20458
- Monaghan, J. J., "Smoothed Particle Hydrodynamics", Annual Review of Astronomy and Astrophysics, **30**, 543–574 (1992), DOI:10.1146/annurev.aa.30.090192.002551

- White, J. L., Chen, Z., "Simulation of Non-Isothermal Flow in Modular Co-Rotating Twin Screw Extrusion", Polym. Eng. Sci., **34**, 229 (1994), DOI:10.1002/pen.760340309
- White, J. L., Keum, J., Jung, H., Ban, K. and Bumm, S., "Corotating Twin-Screw Extrusion Reactive Extrusion-Devolatilization Model and Software", Polym. Plast. Technol. Eng., 45, 539–548 (2006), DOI:10.1080/03602550600554091
- Yang, H.-H., Manas-Zloczower, I., "Flow Field Analysis of the Kneading Disc Region in a Co-Rotating Twin Screw Extruder", Polym. Eng. Sci., 32, 1411–1417 (1992), DOI:10.1002/pen.760321903

Date received: June 18, 2018 Date accepted: October 05, 2018

Bibliography DOI 10.3139/217.3727 Intern. Polymer Processing XXXIV (2019) 2; page 279–289 © Carl Hanser Verlag GmbH & Co. KG ISSN 0930-777X